Epitaxial graphene on SiC(0001) and $^{SiC(000\bar{1})}$: from surface reconstructions to carbon electronics

2009 J. Phys.: Condens. Matter 21 134016

(http://iopscience.iop.org/0953-8984/21/13/134016)

J. Phys.: Condens. Matter **21** (2009) 134016 (12pp) doi:10.1088/0953-8984/21/13/134016

Epitaxial graphene on SiC(0001) and SiC(000$\bar{1}$): from surface reconstructions to carbon electronics

U Starke and C Riedl

Max-Planck-Institut für Festkörperforschung, Heisenbergstraße 1, D-70569 Stuttgart, Germany

E-mail: u.starke@fkf.mpg.de

Received 21 November 2008, in final form 1 January 2009
Published 12 March 2009
Online at stacks.iop.org/JPhysCM/21/134016

Abstract

Graphene with its unconventional two-dimensional electron gas properties promises a pathway towards nanoscaled carbon electronics. Large scale graphene layers for a possible application can be grown epitaxially on SiC by Si sublimation. Here we report on the initial growth of graphene on SiC basal plane surfaces and its relation to surface reconstructions. The surfaces were investigated by scanning tunneling microscopy (STM), low energy electron diffraction (LEED), angle-resolved ultraviolet photoelectron spectroscopy (ARUPS) and x-ray photoelectron spectroscopy (XPS). On SiC(0001) the interface is characterized by the so-called $(6\sqrt{3} \times 6\sqrt{3})$R30° reconstruction. The homogeneity of this phase is influenced by the preparation procedure. Yet, it appears to be crucial for the quality of further graphene growth. We discuss the role of three structures with periodicities $(6\sqrt{3} \times 6\sqrt{3})$R30°, (6×6) and (5×5) present in this phase. The graphitization process can be observed by distinct features in the STM images with atomic resolution. The number of graphene layers grown can be controlled by the conical band structure of the π-bands around the $\bar{K}$ point of the graphene Brillouin zone as measured by laboratory-based ARUPS using UV light from He II excitation. In addition we show that the spot intensity spectra in LEED can also be used as fingerprints for the exact determination of the number of layers for the first three graphene layers. LEED data correlated to the ARUPS results allow for an easy and practical method for the thickness analysis of epitaxial graphene on SiC(0001) that can be applied continuously during the preparation procedure, thus paving the way for a large variety of experiments to tune the electronic structure of graphene for future applications in carbon electronics. On SiC(000$\bar{1}$) graphene grows without the presence of an interface layer. The initial graphene layer develops in coexistence with intrinsic surface reconstructions of the SiC(000$\bar{1}$) surface. In high resolution STM measurements we show atomically resolved graphene layers on top of the (3×3) reconstruction with a Moiré type modulation by a large superlattice periodicity that indicates a weak coupling between the graphene layer and the substrate.

(Some figures in this article are in colour only in the electronic version)

1. Introduction

The physics of graphene has attracted tremendous interest due to its unconventional two-dimensional electron gas and electron transport properties [1–5]. Strictly, graphene stands for a single layer of graphite where the carbon atoms are distributed in a hexagonal lattice layer and form a planar layer due to a sp^2-bonding configuration. However, the notion of graphene is used for single-layer graphene, bilayer graphene and few-layer graphene (up to about ten layers) which can all be seen as different types of two-dimensional crystals [5]. In addition to its own interesting electronic structure, graphene represents the building block of carbon nanotubes or fullerenes. Theoretically, graphene was predicted to be thermodynamically unstable as a free standing layer [6, 7]. Yet, an ever-growing interest in graphene was created when

it was found possible to obtain graphene by micromechanical cleavage of graphite [2]. The π-electrons of the graphene layer form bands that display a linear dispersion cutting through the Fermi energy at the $\bar{K}$-point of the two-dimensional Brillouin zone [1, 8, 9]. Thus, the electron transport is governed by Dirac's (relativistic) equation rather than the Schrödinger equation. A number of unconventional effects, such as new varieties of the quantum Hall effect, relativistic quantum mechanical effects and feasible proposals of graphene-based or carbon nanoelectronics, have been demonstrated, all based on the unconventional two-dimensional electron gas properties [2, 3, 5, 10–13].

Despite the success of the micromechanical cleaving technique, for a practical application the ability to prepare graphene on a large scale and supported on a substrate would be of advantage. The most promising approach in this respect seems to be the controlled graphitization of SiC surfaces [8, 14–18]. After its first realization [19] this procedure has been investigated intensively, yet mainly under the aspect of full graphitization of the surfaces [20–27]. Only recently a graphene-like electronic structure was found for the initial stages developing during this procedure [14, 28]. Investigation of the transport properties of such graphene layers was mainly concentrated on the nominally carbon-terminated SiC(000$\bar{1}$) surface, where the graphene properties are also present in thicker films [28, 29] and the initial growth is of less relevance. On the Si-terminated surface, that is SiC(0001), the two-dimensional electron gas properties of graphene are restricted to very few layers. The initial stage of graphitization on this surface is the $(6\sqrt{3} \times 6\sqrt{3})$R30° reconstruction whose nature has been discussed controversially [14, 19–28, 30, 31]. Originally, it was interpreted as a surface–graphene layer [14]. However, it now seems clear that the specific properties of graphene develop only with the first layer of graphene on top of this $(6\sqrt{3} \times 6\sqrt{3})$R30° structure [8, 9, 18, 30–33]. During the growth of further graphene layers the interface remains unperturbed. An important aspect of the preparation of epitaxial graphene is its homogeneity and the ability to obtain large-area graphene of a defined layer thickness (monolayer, bilayer). In this context an accurate control and understanding of the interface structure is of importance. Yet, the control of the preparation conditions for homogeneous large-area graphene layers is difficult. Another crucial issue is the precise determination of the number of graphene layers on top of SiC(0001). The methods used at present are angle-resolved photoemission spectroscopy (ARPES) at a synchrotron facility [8, 15, 16], scanning tunneling microscopy and spectroscopy (STM/STS) [17, 18, 34, 35], low energy electron microscopy (LEEM) [33, 36, 37], Auger electron spectroscopy (AES) [14, 28], x-ray photoelectron spectroscopy (XPS) [38] and Raman spectroscopy [39–42]. However, these techniques have the limitation that they either depend on a complex experimental set-up (e.g. synchrotron), cannot be applied continuously during the preparation procedure or have a limited accuracy such as due to inaccurate knowledge of the inelastic attenuation of the surface probing electrons in AES or XPS.

As noted above on the SiC(000$\bar{1}$) surface even thicker graphene films can be used and maintain graphene-like properties since the layers grown are rotated with respect to each other, so that no three-dimensional graphite properties develop [28, 29]. The growth of the layers proceeds in a turbostratic manner. At present, the understanding of the initial evolution of mono- or few-layer graphene is still limited, except for investigations of the surface phase diagram before graphene growth [26] and some LEED, ARPES, XPS and STM measurements [38, 43, 44], revealing a coexistence of the initial graphene layers with the less carbon-rich SiC(000$\bar{1}$) surface reconstructions.

In this paper we review the preparation technique of epitaxial graphene in ultrahigh vacuum (UHV) with the first emphasis on a particularly well-ordered interface layer, the so-called $(6\sqrt{3} \times 6\sqrt{3})$R30° reconstruction. We discuss the contribution of three periodicities to this structure that can be observed in different ways, namely $(6\sqrt{3} \times 6\sqrt{3})$R30°, (6×6) and (5×5), and show an optimized preparation procedure to suppress to a large extent the presence of (5×5) domains [18]. On top of this interface layer graphene layers of different thicknesses can be grown that show distinct features in the STM images. The number of graphene layers can be exactly determined by means of angle-resolved ultraviolet photoelectron spectroscopy (ARUPS) with He II excitation at 41.8 eV photon energy from a laboratory-based UV source, thus avoiding the necessity of synchrotron-based ARPES measurements. We show that, even more simply, fingerprints in low energy electron diffraction (LEED) allow for an exact thickness determination for up to three graphene layers on SiC(0001), so that the number of layers can be continuously monitored during the preparation process with high accuracy [33]. Finally, we give a detailed insight into the development of the initial graphene layer on SiC(000$\bar{1}$) using STM, LEED and XPS. We show that the initial graphene layer develops in coexistence with intrinsic surface reconstructions of the SiC(000$\bar{1}$) surface without the formation of an interface layer. As seen in atomically resolved STM images the first graphene layer grows on top of the (3×3) reconstruction with a Moiré type modulation by a large superlattice periodicity that indicates a weak coupling between graphene layer and substrate.

2. Experiment

SiC samples were cut from wafers of different polytype (4H- and 6H-) and polarity, i.e. SiC(0001), the so-called Si-face, and SiC(000$\bar{1}$), the C-face, all on-axis oriented and doped with nitrogen (5×10^{17} to 1×10^{19} cm^{-3} range). All samples were hydrogen-etched in order to remove polishing damage and to chemically passivate the surface. This procedure also generates a regular array of atomically flat terraces of approximately 0.5 μm width [45] as exemplarily displayed by an atomic force microscopy (AFM) image in figure 1(a). After loading into the UHV chamber, the samples were prepared by Si deposition (1 ML min^{-1}) and annealing which allows us to generate several different surface reconstruction phases [26]. The surface structure was investigated using LEED, STM and

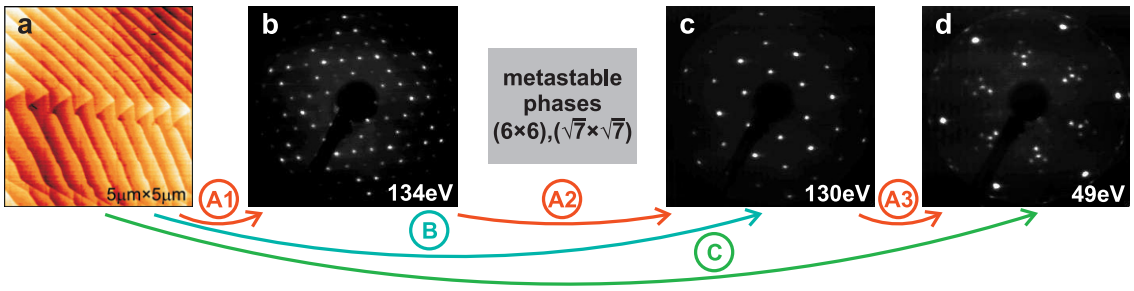

Figure 1. Phase diagram of the SiC(0001) surface: (a) AFM micrograph of 4H-SiC(0001) after H-etching. LEED images of the (b) (3×3), (c) $(\sqrt{3}\times\sqrt{3})$R30° and (d) $(6\sqrt{3}\times 6\sqrt{3})$R30° reconstructions on 4H-SiC(0001). Arrows with encircled process numbers indicate different preparation steps.

AES in a UHV chamber equipped with a sample transfer system between the different methods and sample heating by electron bombardment [46]. Si deposition was carried out using an electron beam evaporator. The electronic structure was analyzed in a separate UHV system with a sample distribution chamber connecting an angle-resolving electron spectrometer chamber with a preparation chamber that is also equipped with LEED, a Si evaporator and sample preparation by resistive heating. The ARUPS experiments were carried out using He II radiation from a monochromatized UV source. The sample manipulator allows for an accurate alignment of both the azimuthal and polar surface orientation to about 0.1°. A hemispherical analyzer equipped with a 2D detector and a charge-coupled device (CCD) camera was used to map the band structure. The spectrometer was also used for XPS experiments with a conventional Mg Kα source. The sample temperatures were determined by an infrared pyrometer. However, it should be noted that the exact temperature measurement in the case of electron bombardment heating is hampered by the glow of the filament which is visible due to the large bandgap of SiC. Temperature values given in this paper are all related to the experiments using resistive heating. It appears that even then the pyrometer values for the same preparation step slightly differ for different samples which we ascribe to subtle influences of different doping levels or the polytype-dependent bandgap.

3. Surface phases and graphitization on SiC(0001)

On the SiC(0001) surface three well-ordered phases can be prepared in addition to a variety of metastable structures [26, 47–51]. The phase diagram is sketched in figure 1. Arrows with encircled process numbers indicate different preparation steps. On the Si-rich side of the phase diagram a well-ordered (3×3) reconstruction develops. This (3×3) phase can be prepared by annealing the hydrogen-etched sample to about 800 °C under simultaneous Si deposition with a flux in the ≈1 ML min^{-1} regime, as indicated by 'A1' in figure 1. An earlier structural analysis by a combined effort of LEED and density functional theory (DFT) revealed that this phase is characterized by an Si adlayer with an additional Si adcluster [52, 53]. As shown in figures 2(a) and (b), in this phase the SiC substrate is covered with a nearly planar Si adlayer with sp^2 type Si bond coordination (less then 0.27 Å buckling within the layer, as indicated in panel (b)

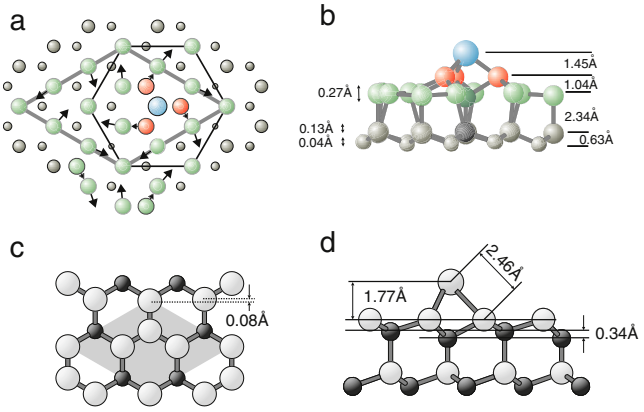

Figure 2. (a) Top and (b) side view of the Si-rich (3×3) reconstruction on SiC(0001). (c) Top and (d) side view of the SiC(0001)-$(\sqrt{3}\times\sqrt{3})$R30° Si adatom reconstruction. Large spheres represent Si atoms, small spheres C atoms. Reproduced with permission from [51]. Copyright 2004 IOP Publishing.

of the figure). On top of this Si layer an Si adcluster in (3×3) periodicity is formed by three Si atoms supporting an additional Si adatom in a threefold coordination [52, 53]. The corresponding (3×3) LEED pattern is displayed in figure 1(b). Heating this surface to approximately 950 °C for about 30 min (with or without Si) results in the development of a $(\sqrt{3}\times\sqrt{3})$R30° phase (process 'A2' in figure 1). During this procedure the surface undergoes a complicated phase transformation with several metastable phases (cf figure 1) coexisting in between [54] until a sharp $(\sqrt{3}\times\sqrt{3})$R30° LEED pattern appears as shown in figure 1(c). The structure of this phase has been determined to be an Si adatom with three bonds to the Si atoms of the topmost SiC bilayer [54]. The close coordination to a carbon atom in the lower sublayer of this SiC bilayer leads to a significant buckling in the substrate, cf figure 2(c) and (d). A further annealing step without additional Si deposition to about 1100 °C (process 'A3' in figure 1) leads to the $(6\sqrt{3}\times 6\sqrt{3})$R30° reconstruction with the LEED pattern shown in figure 1(d). This phase serves as the starting point for the graphene growth and represents an interface or buffer layer for the development of graphene, as we will discuss below. Growth of one to three layers of graphene can be induced by further heating the sample to 1200–1350 °C [18].

An important issue for graphene growth is the homogeneity of the graphene films and, as a prerequisite, the homogeneity of the $(6\sqrt{3}\times 6\sqrt{3})$R30° reconstruction. The structure of this phase has been discussed controversially [14, 19–27, 30, 31, 34, 38] and appears to be dependent on the exact preparation procedure. The process numbers in figure 1 indicate three different possible procedures for the *in situ* (that is, in the UHV chamber) generation of epitaxial graphene which we have investigated in detail with respect to the homogeneity of the resulting films [18]: the first possible pathway (process 'A'), although apparently the most complicated one, is to follow the development of the entire phase diagram as outlined above, which corresponds to the consecutive steps 'A1', 'A2' and 'A3', i.e. to start with an Si-rich surface and prepare one after the other the (3×3), $(\sqrt{3}\times\sqrt{3})$R30° and $(6\sqrt{3}\times 6\sqrt{3})$R30° reconstructions. In a shortcut the C-rich $(6\sqrt{3}\times 6\sqrt{3})$R30° reconstruction can also be obtained by heating the (3×3) phase directly up to 1150 °C. We note that between 1100 and 1150 °C the $(6\sqrt{3}\times 6\sqrt{3})$R30° reconstruction begins to develop but coexists with the $(\sqrt{3}\times\sqrt{3})$R30° structure. The pure $(6\sqrt{3}\times 6\sqrt{3})$R30° reconstruction is accomplished at 1150 °C. Alternatively (process 'B') it is possible to start with an initial annealing step at 950 °C in a flux of Si (≈1 ML min^{-1}) by which the $(\sqrt{3}\times\sqrt{3})$R30° structure develops. By further heating of this surface without Si addition the $(6\sqrt{3}\times 6\sqrt{3})$R30° phase can be realized immediately. The simplest method and one still quite frequently applied is to directly anneal the *ex situ* hydrogen-etched sample to reach the $(6\sqrt{3}\times 6\sqrt{3})$R30° phase and subsequently grow graphene layers [18]. This method corresponds to process 'C' in figure 1.

4. Homogeneity of the interface layer

The homogeneity and consistency of the buffer layer depends on which preparation procedure is applied. Figure 3 displays LEED patterns of the $(6\sqrt{3}\times 6\sqrt{3})$R30° reconstruction of 4H-SiC(0001) corresponding to preparation by the three procedures 'A', 'B' or 'C' combined with an additional annealing step at around 1100 °C [18]. All three patterns which are quite similar are normally identified as having a $(6\sqrt{3}\times 6\sqrt{3})$R30° periodicity. Yet, a detailed inspection of the spots in the vicinity of the $\frac{1}{3}$ diffraction order, as displayed in the enlarged sections on the right of the three LEED patterns (shown both in normal and reverse contrast for clarity), reveals a more complex scenario. The spot indicated by the arrow in the reverse contrast image is at the $(\frac{1}{3},\frac{1}{3})$ position which is characteristic of the $(\sqrt{3}\times\sqrt{3})$R30° structure which is still present coexisting with the $(6\sqrt{3}\times 6\sqrt{3})$R30° phase. We noted above that the $(6\sqrt{3}\times 6\sqrt{3})$R30° phase requires temperatures above 1150 °C to develop in a pure state. The $(\frac{1}{3},\frac{1}{3})$ spot gradually disappears with increasing temperature as the corresponding domains disappear, too. The spots on the triangle marked in green (light gray) have distances of $\frac{1}{6}$ of the substrate's reciprocal surface unit-mesh vector. However, since the $(\frac{1}{3},\frac{1}{3})$ position in the center of the triangle is part of a (6×6) grid on the SiC(0001) surface, it is clear that the spots on the green (light gray) triangle are shifted with respect to the (6×6) grid and belong to a true $(6\sqrt{3}\times 6\sqrt{3})$R30° grid.

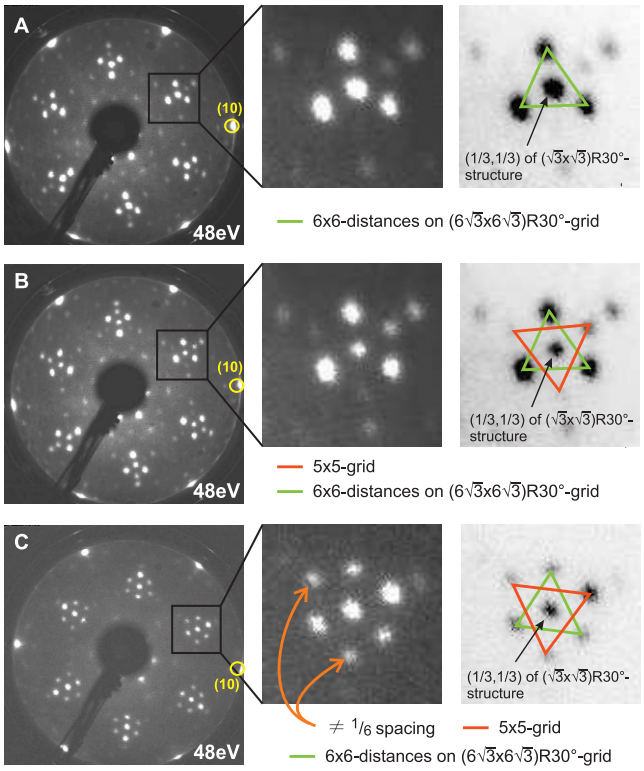

Figure 3. LEED patterns of the $(6\sqrt{3}\times 6\sqrt{3})$R30° reconstruction of 4H-SiC(0001) for three different preparation procedures labeled A, B and C (see text for details), with an additional annealing step at a temperature of about 1100 °C. Note that at this temperature there are still coexisting $(\sqrt{3}\times\sqrt{3})$R30° patches present. Using procedure A the Si-rich (3×3) structure is annealed, using procedure B the $(\sqrt{3}\times\sqrt{3})$R30° structure is heated up and, during procedure C, the preparation is conducted by annealing an *ex situ* sample. Spots on a $(6\sqrt{3}\times 6\sqrt{3})$R30° grid as well as on a (5×5) grid can be observed exhibiting different relative intensities. Reproduced with permission from [18]. Copyright 2007 by the American Physical Society.

Accordingly, the surface cannot have a (6×6) periodicity as could be assumed from the (6×6) corrugations often observed in STM (see below). In the case of preparation procedures 'B' and 'C' additional spots appear, namely the spots indicated by the triangles marked in red (dark gray). However, their position deviates from the $(6\sqrt{3}\times 6\sqrt{3})$R30° grid. The spots have a larger mutual distance than the spots on the green (light gray) triangle and accordingly cannot belong to the $(6\sqrt{3}\times 6\sqrt{3})$R30° grid. They rather have to be attributed to a (5×5) grid, as can be confirmed with LEED data at different energies. The absolute intensity of the spots on the (5×5) grid are different for the different preparation procedures, and almost absent for preparation procedure 'A', which suggests different amounts of (5×5) domains resulting for the different preparation procedures. We note that spots at different diffraction order on the (5×5) grid have different intensities, which is due to multiple scattering effects. However, the relative spot intensities of the red (dark gray) triangle are equal for the different procedures, indicating the origin from the same kind of surface structure within the (5×5) domains.

The role of the (5×5) periodicity in the different preparation procedures can be elucidated using STM [18]. Figure 4

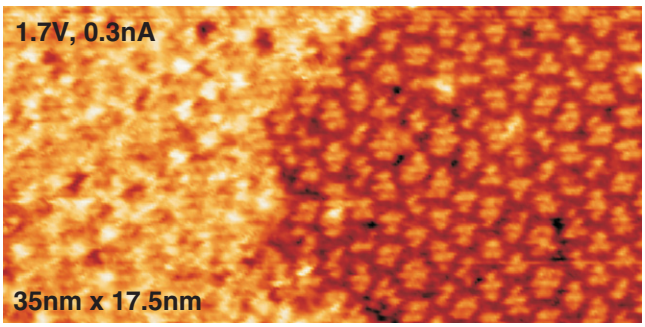

Figure 4. STM images of the $(6\sqrt{3} \times 6\sqrt{3})$R30° reconstruction on 4H-SiC(0001) typically show a (6×6) corrugation as visible on the left-hand side of the figure. They often appear in coexistence with (5×5)-periodic patches (right-hand side) that are formed by somewhat disordered structural elements. The latter are responsible for the deviations from the $(6\sqrt{3} \times 6\sqrt{3})$R30° periodicity in the LEED patterns shown in figure 3 and their amount depends on the preparation procedure.

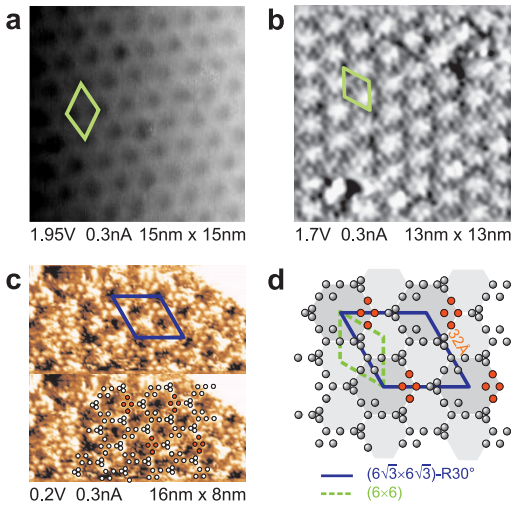

Figure 5. Atomically resolved STM images (a) at $U_{tip} = 1.95$ V, (b) at $U_{tip} = 1.7$ V and (c) at $U_{tip} = 0.2$ V. Whereas panels (a) and (b) show a quasi-(6 × 6) corrugation, panel (c) exhibits atomically resolved rings of adatoms of two different sizes. In the lower part of panel (c) which displays the same surface area as the upper part the individually resolved atomic-like protrusions are indicated. The arrangement of the atoms or atomic clusters, together with the corresponding unit cells, is displayed in panel (d).

shows a filled state STM image of the $(6\sqrt{3} \times 6\sqrt{3})$R30° reconstruction exhibiting two different periodicities, a (6×6) honeycomb structure on the left-hand side and a (5×5) structure on the right-hand side of the panel. The (5×5) structure is characterized by clusters with a varying number of atoms. We observe this structure for all three preparation procedures independent of the annealing temperature of the $(6\sqrt{3} \times 6\sqrt{3})$R30° reconstruction. Only the number and fraction of (5×5) domains is largest for the *ex situ* prepared sample (procedure 'C'), in full agreement with the stronger intensity level of the (5×5) LEED spots and almost vanishing intensity for procedure 'A'. Nevertheless, we should note that, according to our STM measurements, there are always (5×5) patches present even when starting the preparation from the Si-rich (3×3) phase. We note that a (5×5) reconstruction was also previously reported in the framework of the $(6\sqrt{3} \times 6\sqrt{3})$R30° phase [20] based upon LEED and STM investigations. In that case, an *ex situ* sample was annealed without simultaneous Si deposition.

5. Structure of the $(6\sqrt{3} \times 6\sqrt{3})$R30° phase

The atomic and electronic structure of the interface layer is, of course, important for the structural attachment and the electronic properties of the graphene layers on top. As outlined above, a homogeneous development of the layer can be greatly enhanced by preparation under Si-rich conditions. Nevertheless, the crystallographic structure of the $(6\sqrt{3} \times 6\sqrt{3})$R30° reconstruction is not completely resolved up to now. From our ARUPS results (not shown) and from synchrotron ARPES measurements [9, 38] it is clear that the buffer layer has no continuous π-bands at the $\bar{K}$-point so that it does not represent an electronically decoupled graphene layer. It acts, however, as a precursor phase of graphitization. The interface layer comprises a partially covalent carbon layer, as it already exhibits σ-bands, which can also be seen in graphene [9, 38]. In STM the $(6\sqrt{3} \times 6\sqrt{3})$R30° structure is often imaged with an apparent (6×6) periodicity in particular at high tunneling bias, as shown in figures 5(a) and (b). Depending on the bias voltage, this 'quasi'-(6×6) corrugation can appear like rings in a honeycomb pattern (at 1.95 V tip bias, panel a) or as a hillock structure (at 1.7 V, panel (b)) which indicates a complex electronic structure of the phase [18, 22, 55, 56]. Only at small tunneling voltages can one identify the true $(6\sqrt{3} \times 6\sqrt{3})$R30° periodicity, although it is difficult to obtain a clear image. At a tunneling voltage of 0.2 V two types of rings with slightly different size can be resolved that are formed by what appears to be individual atoms. We note that the STM of course images high charge densities, which for simplicity we treat as atomic positions in the present context. Three additional atom-like structures are present in every third ring whereby each atom is part of a diamond of four atoms. The lower part of panel (c) displays the same surface area as the upper part. Diamonds oriented in the same direction are marked in red (dark gray) in this lower part of panel (c) and are repeated only with $(6\sqrt{3} \times 6\sqrt{3})$R30° periodicity, so that three rings (one larger and two smaller ones) form the $(6\sqrt{3} \times 6\sqrt{3})$R30° unit cell. The positions of the atom-like features are elucidated in panel (d) of the figure by a sketch of the rings with their different sizes and the three additional atoms (or atomic clusters). The unit cells of the (6×6) and the $(6\sqrt{3} \times 6\sqrt{3})$R30° periodicity are also indicated. With this real space arrangement the periodicity of the LEED patterns can be explained which is not possible assuming a (6×6) structure only. Of course, this sketch resolves only a few atoms of the $(6\sqrt{3} \times 6\sqrt{3})$R30° surface, its complete atomic structure is still unresolved (the closest distance of atoms resolved here is $\sqrt{3}$ times the SiC unit cell vector length). This fact, however, should not come as a surprise since one $(6\sqrt{3} \times 6\sqrt{3})$R30° unit cell contains 108 Si and 108 C atoms per SiC bilayer or 338 atoms in a graphene layer. The (1×1)

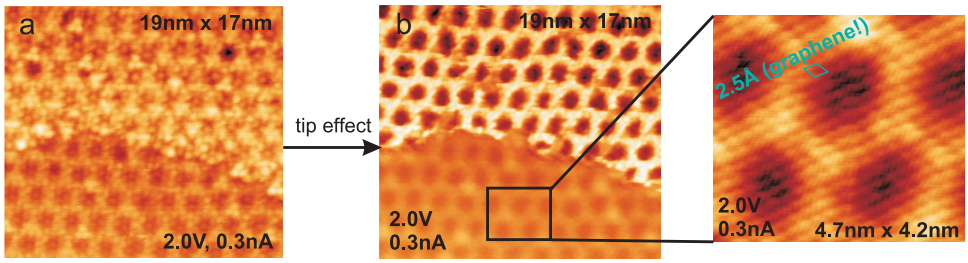

Figure 6. Atomically resolved STM images of the $(6\sqrt{3} \times 6\sqrt{3})$R30° reconstruction on 4H-SiC(0001) showing (6×6) corrugations with two different contrasts for two different tip conditions shown in panel (a) and panel (b). Only for the tip condition in panel (b) can graphene on top of the $(6\sqrt{3} \times 6\sqrt{3})$R30° reconstruction be resolved (enlargement of the lower part of the STM image). The annealing temperature was around 1220 °C.

unit vectors of SiC(0001) are 3.08 Å and the unit vectors of graphene are 2.46 Å long, so that the $(6\sqrt{3} \times 6\sqrt{3})$R30° supercell has a 32 Å side length, as indicated in panel (d).

Several models exist in the literature for the structure of the $(6\sqrt{3} \times 6\sqrt{3})$R30° phase. Some of them do not even consider the $(6\sqrt{3} \times 6\sqrt{3})$R30° structure as an inherent surface reconstruction of SiC(0001). So, Owman and Mårtensson proposed the coexistence of a (6×6) and an incommensurate $(\sqrt{2.1} \times \sqrt{2.1})$R30° phase [20], which is not in agreement with the interpretation of the LEED and STM results as described above. It has been argued that the LEED diffraction image shows a Moiré pattern of graphite and the SiC substrate [14, 19, 24]. However, such an interpretation is inconsistent with the valence band structure where a continuous π-band is absent at the $\bar{\text{K}}$-point as seen by ARPES [8, 9, 38] or our ARUPS data. Nevertheless, a honeycomb-like arrangement of carbon atoms in this phase could be envisioned. However, within this layer atoms with bonds to the substrate and atoms with dangling bonds must form a complex pattern to accommodate the STM results [34]. The overall picture is a partially covalent carbon layer with a geometrical structure close to a graphene sheet, yet at least partially connected to the substrate by covalent bonds [30, 31, 34, 38]. Recently, from STM the presence of Si clusters was proposed [56], which, however, awaits confirmation, e.g. by core level photoemission. In our group, we are currently attempting an LEED structure analysis of this phase.

6. Growth and identification of graphene layers

The identification and control of a certain number of graphene layers to be grown on top of SiC(0001) is a key factor to obtain high quality graphene samples by this method and has, for a long time, been difficult. Layer thickness measurements were carried out using AES [14, 28] or XPS [38]. However, the diameter of the probing beam of these methods is much larger than the terrace size with a definite number of graphene layers so that an average value is always obtained. The reliability of using the Si/C intensity ratio in AES or XPS also suffers from inaccurate knowledge of the inelastic attenuation of the electrons probing the surface. Synchrotron-based ARPES has been used quite successfully to determine the layer thickness [8, 9, 32], but it requires access to a dedicated facility and thus is applicable only in certain cases and at certain times. Also, the preparation typically cannot be carried out in the same UHV chamber as the ARPES analysis. We have recently shown that Raman spectroscopy, which offers a much smaller beam diameter than the other techniques mentioned, can be used to identify epitaxial graphene layers on SiC [42]. However, its application even requires the removal of the sample from the UHV growth chamber, so that it can only be used for post-growth assessment. It would certainly be desirable to find an easy and exact way for the determination of the number of graphene layers that can be used in the home laboratory and, in particular, continuously during the preparation procedure. In the following we use ARUPS with a laboratory-based UV source to calibrate the number of graphene layers grown and elaborate how LEED intensity spectra, which can be obtained directly in the growth chamber, have the potential to be used as fingerprints and so offer a solution to this problem.

6.1. Imaging the graphene unit cell

However, we start with the identification of the graphene layers on the nanometer scale using results from STM measurements at room temperature. We use a sample that was annealed at a temperature around 1220 °C which in the STM shows terraces of apparently different thicknesses [18]. In figure 6 we compare the images of the same surface area for two different tip conditions that contrast differently on the corresponding terraces. The first tip condition allows for atomic resolution of the $(6\sqrt{3} \times 6\sqrt{3})$R30° reconstruction, while the second one seems to allow only for reduced quality at a first glance. However, scaling down the scanning area leads to atomic resolution of graphene on top of the $(6\sqrt{3} \times 6\sqrt{3})$R30° surface reconstruction even with a room temperature STM. Yet, this is only the case for the region with the reduced contrast. The unit cell size of about 2.5 Å corresponds to that of graphene. Since we observe only one of the two carbon atoms comprising the graphene unit cell we can identify this surface region as (at least) bilayer graphene. The Bernal stacking of two graphene sheets leads to the observation of such a diamond-shaped lattice [57]. The crucial point that should be emphasized is that the visibility of the graphene layers strongly depends on the actual tip condition, thus

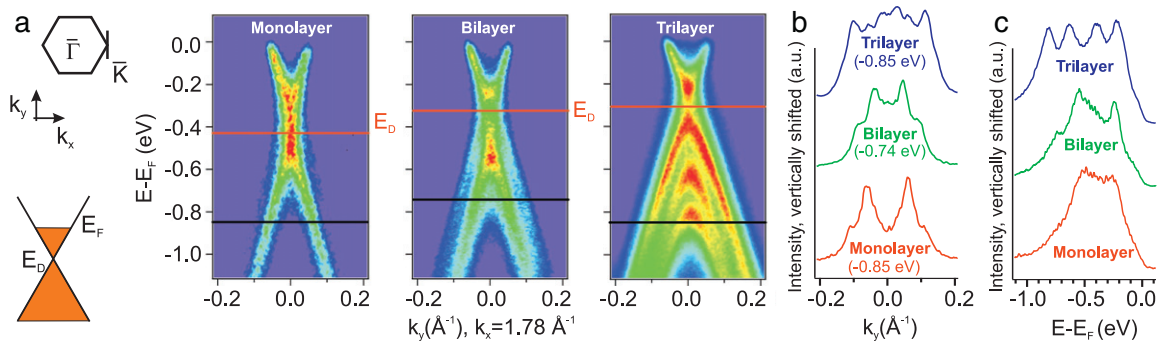

Figure 7. Band structure of monolayer, bilayer and trilayer graphene epitaxially grown on 4H-SiC(0001) near the $\bar{K}$-point obtained by ARUPS using He II radiation. (a) Photoemission images measured in the k_y direction (as indicated on the upper left) revealing the different branches of the π-bands for different layer numbers. The position of the Dirac energy (see lower sketch on the left) is indicated. (b) Momentum distribution curves extracted from the images at the energies indicated by the black lines in panel (a) and noted under the curves, integrated over 30 meV. (c) Energy distribution curves extracted at $k_y = 0$ integrated over 0.01 Å^{-1}.

complicating the determination of the number of graphene layers by means of STM. In the upper part of figure 6 the higher contrast in the STM image represents a lower coverage with graphene. It is presumably a monolayer where, due to the high bias voltage, the graphene layer is nearly transparent for the tunneling current and the interface structure can be imaged [17, 34, 58, 59]. Nevertheless, it may be even no graphene layer at all, although it is likely that a single graphene layer can also be identified by using a different bias voltage. We note that mono-and bilayer graphene have recently also been identified using scanning tunneling spectroscopy (STS) at cryogenic temperatures [17, 35, 58].

6.2. Band structure

Apart from the identification of the atomic structure of graphene layers on a microscopic level modern photoemission experiments allow for directly imaging the band structure of graphene on a probing area of ≈1 mm^2 and smaller. The number of π-band branches in the vicinity of the $\bar{K}$-point depends on and is equal to the number of graphene layers [60] which can be resolved in photoemission [8]. Figure 7 displays ARUPS data taken with an He lamp revealing the electronic structure in the vicinity of the $\bar{K}$-point of the Brillouin zone of graphene for annealing temperatures of 1200, 1275 and 1350 °C [33]. The sketch in panel (a) defines the $\underline{k}_{\parallel}$-mapping direction. The E versus $\underline{k}_{\parallel}$ plots in panel (a) clearly show that the development of the π-bands is strongly dependent on the number of graphene layers. The data compare well to previous reports based on synchrotron data [8, 15, 16]. By counting the number of π-bands one, two and three graphene layers can clearly be distinguished. For a quantitative evaluation, momentum and energy distribution curves (MDC and EDC) for mono-, bi- and trilayer graphene are displayed in figures 7(b) and (c). These results show that a distinction based on angle-resolved valence band spectroscopy can be achieved even using UV light from an He II excitation in the home laboratory. Consistent with previous reports [15, 16] we find that the Dirac point is shifted below the Fermi energy by 430 meV for monolayer, 320 meV for bilayer and 300 meV for trilayer graphene and also the reported [15, 16] energy gap at the Dirac energy for bi- and trilayer graphene can be observed. Using 4H- and 6H-SiC samples we could verify that the band structure for epitaxial graphene shows no polytype dependence [33, 42].

6.3. LEED fingerprints

Although the determination of the number of graphene layers by means of ARUPS would be a rather convenient method, it cannot be applied during preparation, and a machine with the appropriate precision might not normally be at hand. However, a LEED optics is available in practically every preparation chamber. During the growth of graphene layers of different thicknesses both the LEED pattern of the $(6\sqrt{3} \times 6\sqrt{3})\text{R}30°$ reconstruction as well as the intensity spectra of the first-order diffraction spot of graphene (marked in green (light gray) in figure 8) display characteristic variations with increasing temperature [18]. The calibration of these changes with the ARUPS data shown in figure 7 allows for an unambiguous assignment of the LEED intensities to the number of graphene layers, as shown in figure 8. Thus, specific features in the intensity spectra, which are highlighted (yellow/gray ovals) in the figure and which are generated by the complex multiple scattering processes in LEED, allow for an accurate determination of the number of graphene layers using LEED alone and can be used as fingerprints for the control of the growth process [33]. Not every LEED system may permit the acquisition of such intensity spectra, but already the LEED pattern at 126 eV allows for an approximate determination of the number of layers by comparing the relative intensity of the 'graphene spot' to that of the surrounding spots in the $(6\sqrt{3} \times 6\sqrt{3})\text{R}30°$ pattern as shown in figure 8. We note that epitaxial graphene on 6H-SiC(0001) results in the same LEED spectra [61], a finding that corroborates that—with the same preparation procedure—the polytype has no influence on the structural and electronic properties of epitaxial graphene on SiC.

The feasibility and practicability of a very precise calibration of the graphene layer thickness by ARUPS and LEED suggest a large-area production of graphene samples with a pre-defined, uniform number of layers. However,

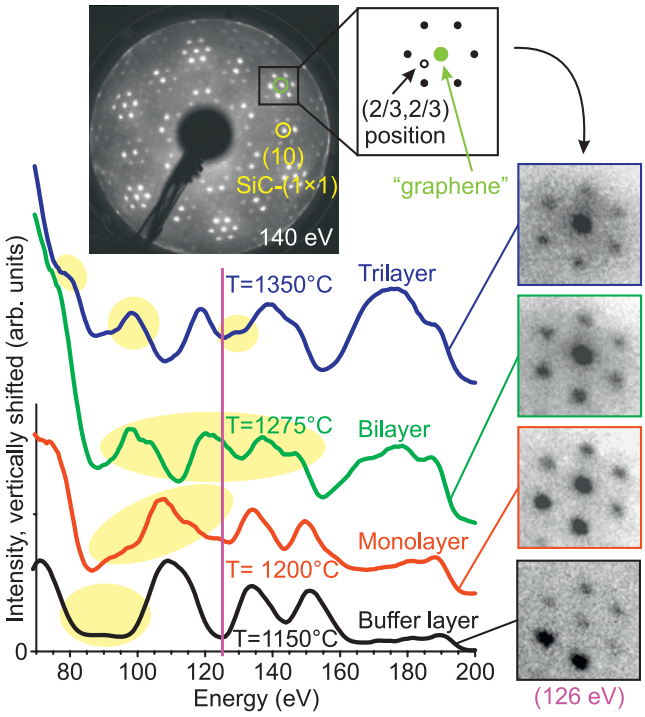

Figure 8. LEED spot intensity spectra for different numbers of epitaxial graphene layers grown (at the indicated temperatures) on 4H-SiC(0001). As indicated in the inset, the spectra were obtained for the green (light gray) marked spot of the $(6\sqrt{3} \times 6\sqrt{3})$R30° reconstruction, which corresponds to the unit cell of graphene. The first-order diffraction spot for the SiC substrate is indicated in the LEED pattern in yellow (white) and the position of the (2/3, 2/3) spot of the $(6\sqrt{3} \times 6\sqrt{3})$R30° reconstruction in the inset. Yellow (light gray) patches indicate fingerprint-like features in the spectra that allow the unambiguous determination of the number of graphene layers. LEED patterns at 126 eV are shown on the right, also allowing for a discrimination.

a closer look on a microscopic length scale, e.g. by STM [18, 34], demonstrates that there is still a long way ahead towards homogeneous growth conditions on a large area since individual graphene patches are continuous only on a length scale of about 100 nm. LEEM, in particular, is perfect for imaging the homogeneity of epitaxial graphene on the micrometer scale. In the low energy regime, the maxima and minima of the (0, 0) diffraction spot of graphene allow a microscopic distinction of graphene patches with a different number of layers [33, 36, 37]. The LEEM experiments show that growth takes place on a micrometer scale or below [33] and the next layer of graphene develops before the previous one has been filled and closed [36, 37]. This shows that improved growth conditions have to be developed, but the process can be perfectly monitored by LEEM. Recently, it has been suggested to use a high pressure growth process which allows us to obtain larger and more homogeneous graphene patches [62], a technique that has also been used to grow thick graphene layers on SiC(000$\bar{1}$) [28].

7. Epitaxial graphene on SiC(000$\bar{1}$)

Epitaxial graphene grown on the carbon face of the basal plane surfaces of SiC exhibits completely different growth characteristics than graphene on the silicon face. Most of the transport measurements have so far been conducted on SiC(000$\bar{1}$) [28] whereas the structural and electronic properties have more extensively been analyzed on SiC(0001). The phase diagram of SiC(000$\bar{1}$) has a similar complexity as the one on SiC(0001). Also similar preparation procedures were applied although the annealing temperatures are generally higher on SiC(000$\bar{1}$). The sequence of surface reconstructions, however, is completely different [26, 63] and is shown in figure 9. The Si-rich side of the phase diagram starts with a (2×2) phase with an LEED pattern as shown in figure 9(a) which is denoted $(2 \times 2)_{Si}$ in order to distinguish it from a more carbon-rich $(2 \times 2)_C$ phase (see below). The $(2 \times 2)_{Si}$ phase develops upon annealing in Si flux at about 1150 °C (indicated as process 'A' in figure 9). This procedure is also used in order to remove surface oxides from the hydrogen-etched samples. Further annealing at 1050 °C (process '1') results in a (3×3) reconstruction, cf figure 9(b). The (3×3) reconstruction can also be observed after directly annealing the hydrogen-etched sample up to 1000 °C (process 'B'). Heating of the (3×3) structure (at 1075 °C, process '2') leads to the carbon-rich $(2 \times 2)_C$ phase (LEED pattern in figure 9(c)) which, in most cases, can only be prepared in coexistence with the (3×3) reconstruction [63, 64]. We note that the $(2 \times 2)_C$ is the only phase on SiC(000$\bar{1}$) for which the atomic structure of the surface (an Si adatom model) has been resolved [65]. Further heating at temperatures of at least 1150 °C (process '3') leads to a graphitic phase with (1×1) spots of the SiC substrate and ring-like diffraction features from the graphite layer as shown in figure 9(d). However, before observing a pure graphitic (1×1) structure graphene already coexists with the (3×3) and $(2 \times 2)_C$ phases [38, 44]. Figure 10 displays an LEED pattern of this first stage of graphene growth. It shows sharp and intense spots that correspond to both the (3×3) and the $(2 \times 2)_C$ periodicity but also quite weak graphitic diffraction rings that are located close to the $(\frac{2}{3}, \frac{2}{3})$ position of the SiC substrate, as shown in the enlarged section in the figure. The position of these graphitic intensities suggests that the graphene is rotated by 30° with respect to the SiC substrate, as is the case for SiC(0001). However, the fact that the LEED pattern does not show a single spot but rather a ring indicates that graphene patches are existing in domains of different orientations with respect to the substrate.

The essential differences between the graphitization processes on both polarities of SiC{0001} basal plane surfaces already arise in these initial stages of the graphitization process. In the case of SiC(0001) the $(6\sqrt{3} \times 6\sqrt{3})$R30° reconstruction corresponds to a covalently bound graphene layer so that it can act as an electronically inactive buffer layer as outlined above. Such a precursor phase of graphitization is missing for SiC(000$\bar{1}$). The existence of rotated domains can already be seen as an indication of the absence of a strongly bonded first graphene layer, which has recently been confirmed by photoemission data [38]. Spectra of the C 1s core level, in particular, allow for a detailed analysis of differently bound carbon atoms as shown in figure 11 for 0.3, 0.6 and 0.8 ML graphene with the thickness evaluated by consideration of the layer-dependent electron attenuation. In contrast to

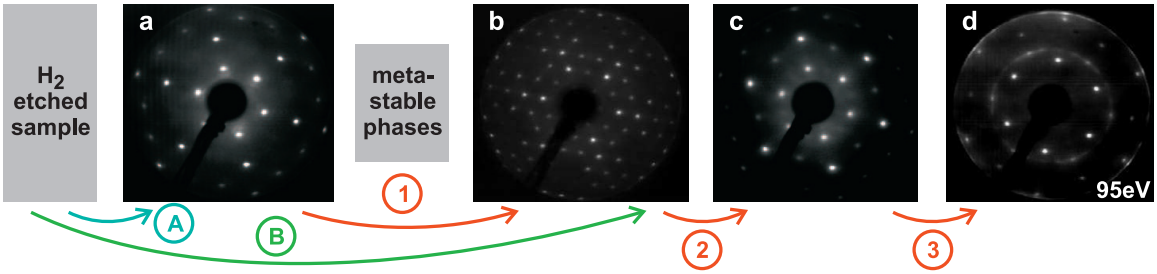

Figure 9. Phase diagram of the SiC(000$\bar{1}$) surface with LEED images of (a) the $(2 \times 2)_{Si}$, (b) the (3×3) and (c) the $(2 \times 2)_C$ reconstruction phase as well as (d) a graphitic surface. Arrows with encircled process numbers indicate different preparation steps.

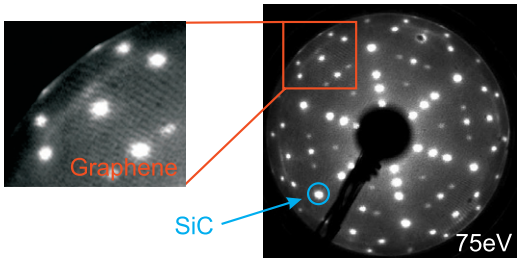

Figure 10. LEED pattern at 75eV showing a coexistence of the (3×3) and the $(2 \times 2)_C$ phase with a graphitic $(1\times1)_{graphitic}$ structure on SiC(000$\bar{1}$). The graphene does not show a distinct spot but rather a ring-like structure as shown in the inset.

epitaxial graphene on SiC(0001), where three components can already be observed for the buffer layer reconstruction, only two components can be resolved on SiC(000$\bar{1}$). This also holds for higher graphene coverages [38], which are not shown here. The SiC bulk component appears at 282.8 eV binding energy and the graphene-related component at 284.6 eV. The binding energy of the latter slightly decreases for higher coverages, thus approaching that of graphite (284.4 eV). As soon as the graphitization starts there is no indication for a covalent bonding of graphene to the SiC substrate. For graphene on SiC(0001) the covalent bonding gives rise to two surface-related components in the buffer layer, which remain unperturbed during the graphene growth [38]. As further graphene layers are starting to grow from the bottom, the orientation of the graphene layers will always be the same as their growth direction is imprinted by the buffer layer. Due to the weak coupling of graphene in the case of SiC(000$\bar{1}$) the graphene can grow in rotated domains which results in a turbostratic growth mode [43, 66].

It should be noted that density functional theory calculations [30, 31] as well as studies with inverse photoemission [67] and x-ray reflectivity [29, 66] have claimed a strong interaction between the first graphene layer and the SiC(000$\bar{1}$) substrate. Deeper insight on a microscopic level can be given by STM. It can be directly analyzed how and on what surface reconstruction(s) the graphene growth takes place. We investigate an early graphene stage where still considerable contributions from the $(2 \times 2)_C$ and in particular the (3×3) reconstructions are present. STM data, where patches of both phases can be seen, are presented in figure 12. Figure 12(a) shows a large scale STM micrograph highlighting

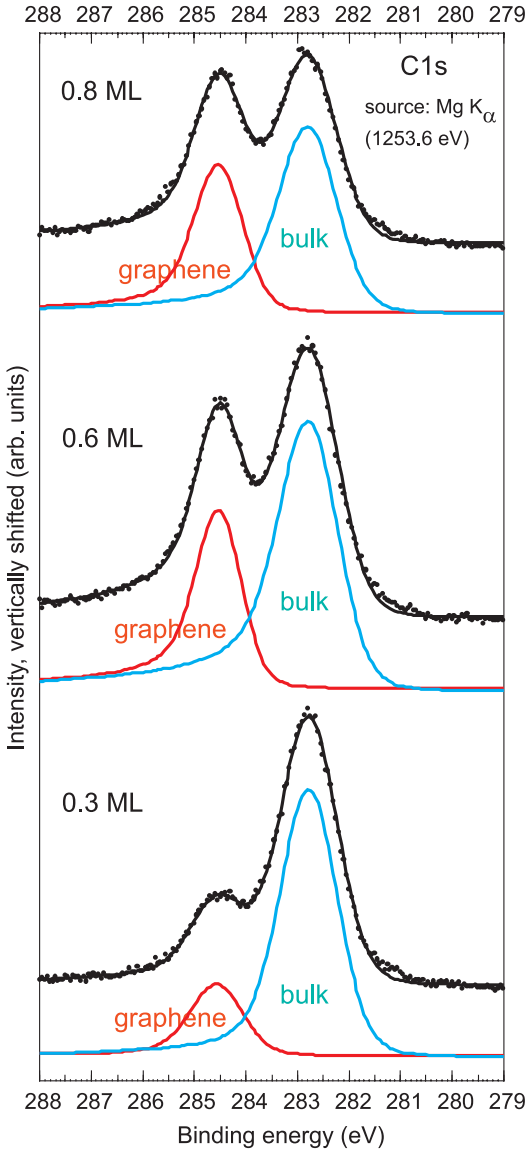

Figure 11. C 1s core level spectra for the initial stages of graphitization of SiC(000$\bar{1}$) with different graphene layer thicknesses as determined from layer-dependent electron attenuation. The graphene is growing without the formation of an interface layer.

the fact that, as for SiC(0001), UHV grown epitaxial graphene on SiC(000$\bar{1}$) does not exhibit a large homogeneity. The LEED pattern corresponding to the STM images displays

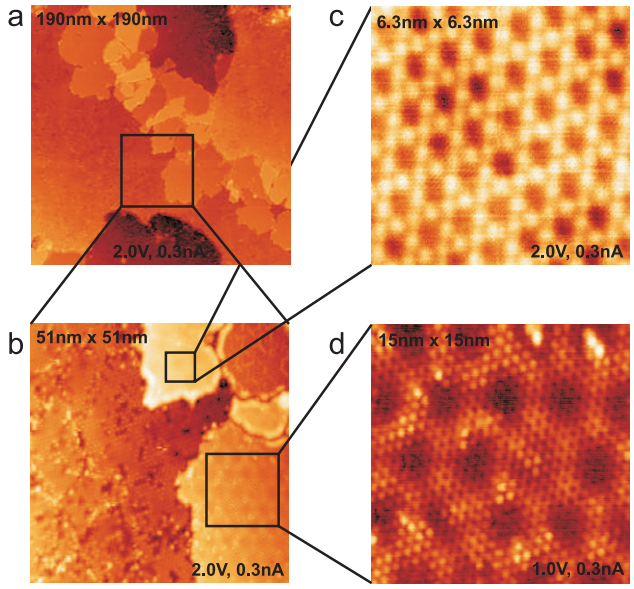

Figure 12. STM micrographs for the initial stages of graphitization on SiC(000$\bar{1}$). (a) Large-area image, which shows the inhomogeneous growth characteristics. (b) Overview of the different surface reconstructions: the pure (3×3) phase and the (2×2) and (3×3) phases covered with graphene showing a Moiré type superlattice. (c) Enlarged scan of the graphene-covered (3×3) phase (panels (a)–(c): $U_{\mathrm{tip}} = 2.0$ V). (d) Enlarged scan of the graphene-covered (2×2) phase ($U_{\mathrm{tip}} = 1.0$ V).

an even weaker graphitic ring than shown in figure 10 and mainly consists of the (3×3) reconstruction (not shown). Correspondingly, most of the area in figure 12(a) is covered by the (3×3) structure. Panel (b) shows a smaller area of this surface with higher resolution as indicated by the zoomed sketch between panels (a) and (b). Here, the left-hand side is covered with the (3×3) phase in particular. On the right-hand side in panel (b), however, the two surface reconstructions $(2 \times 2)_{\mathrm{C}}$ and (3×3) can be observed with different superlattices on top, as pointed out by the enlargements in panel (c) and (d). Panel (c) displays the (3×3) reconstruction with a superlattice periodicity of 4.2 nm and panel (d) shows the $(2 \times 2)_{\mathrm{C}}$ reconstruction with a superlattice periodicity of 3.6 nm. The periods of these superlattices are related to the rotation of the graphene-like overlayers with respect to the SiC substrate and can be seen as Moiré patterns [44]. Such superlattices have already been observed in earlier STM studies on the $(2 \times 2)_{\mathrm{C}}$ phase [63–65] but could not be directly linked to the growth of graphene. For monolayer graphene on SiC(0001) it is known that its visibility depends on the bias voltage [17, 34, 58, 59]. The STM micrographs in figures 12(a)–(c) have been taken at high bias. For these values the graphene layer is transparent for tunneling and only the bare surface reconstructions, which have earlier been analyzed extensively [63–65, 68], can be observed. At the chosen tunneling bias of 2.0 V (tip voltage) the (3×3) structure displays a regular array of hexagonal holes. For low tunneling bias, however, a single protrusion per unit cell can be resolved, which is shown in figure 13. Furthermore the graphene layer can be seen as a honeycomb pattern and

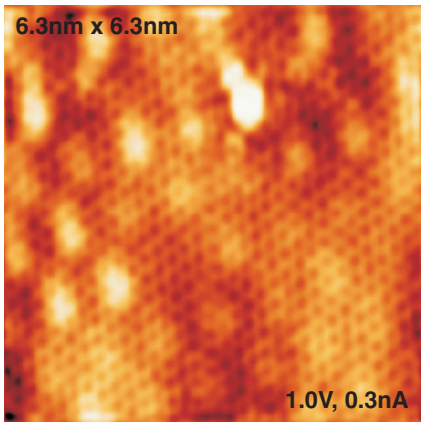

Figure 13. Atomically resolved graphene layer covering the (3×3) reconstruction acquired at a tip bias of +1.0 V. The graphene layer is rotated by 18° with respect to the substrate.

the graphene unit cell can indeed be resolved. The fact that every graphene atom of the unit cell can be imaged is another indication for monolayer graphene [17, 34, 57–59]. The rotation of the graphene unit cell with respect to the SiC substrate amounts to 18°. These observations confirm the picture of a weak interaction of the first graphene layer on SiC(000$\bar{1}$). Furthermore, Hiebel *et al* have concluded from STM data that the substrate-overlayer coupling is a bit stronger for the $(2 \times 2)_{\mathrm{C}}$ phase [44] but still much smaller than the covalent bonding of the first graphitic layer on the Si face, which is represented by the $(6\sqrt{3} \times 6\sqrt{3})$R30° reconstruction.

For a higher graphene coverage the SiC surface reconstructions cannot be resolved any more. Instead, different kinds of Moiré patterns can be observed which corroborate the proposal of a turbostratic growth mode on SiC(000$\bar{1}$) [43]. The rotational disorder leads to an electronic decoupling of the graphene layers, thus preserving some unique properties of monolayer graphene even in thicker films [14, 28, 29]. Despite its complicated graphene growth characteristics, the C-face of SiC{0001} represents an attractive support for potential graphene-based or carbon electronics.

8. Conclusion and outlook

The formation of graphene on SiC basal plane surfaces and their electronic and atomic structure were investigated using STM, LEED, ARUPS and XPS. In addition to the properties of graphene layers the initial growth process and the extent of the coupling and interface formation to the substrate were studied for the two basal plane orientations. On SiC(0001) a precursor phase of graphitization develops which is composed of a carbon layer and does not yet exhibit the typical properties of graphene. That is the so-called $(6\sqrt{3} \times 6\sqrt{3})$R30° reconstruction which can be viewed as an interface or buffer layer. It is sometimes called the zero layer in view of it not yet being graphene. The homogeneity of this layer depends on the exact preparation procedure and is disturbed by the coexistence of (5×5) patches as visible in LEED and STM. We argue that the amount of disorder in the interface layer influences

the characteristics of subsequent graphene growth and propose an optimized procedure for preparation in UHV. A partial structural model for the $(6\sqrt{3} \times 6\sqrt{3})$R30° reconstruction is outlined based on low-bias STM data [18]. In agreement with other work [30, 31, 34, 38] the model involves covalent bonds connecting the interface layer to the substrate which in fact prevent the formation of the conical π-band dispersion characteristic for graphene. Graphene layers on top of the $(6\sqrt{3} \times 6\sqrt{3})$R30° reconstruction lead to a decreased contrast in the STM images. Under certain tip and bias conditions the graphene unit cell can directly be observed even at room temperature [18]. The number of π-band branches in the vicinity of the $\bar{\text{K}}$-point is an unambiguous label for the number of graphene layers and can be resolved by ARUPS using UV light from a laboratory-based He excitation source [33]. The progressing graphitization also results in significant changes in the LEED intensity spectra. Calibrated to the valence band data from ARUPS the LEED intensities can be used as fingerprints to facilitate a precise *in situ* control of the growth of epitaxial graphene on SiC(0001) with an exactly defined number of layers [33].

On SiC(000$\bar{1}$) the initial graphene layer develops in coexistence with the intrinsic surface reconstructions without the presence of an interface layer. STM resolves the graphene structure directly on top of the (3×3) reconstruction with a Moiré type modulation by a large superperiodicity. The corresponding rotational orientation of the graphene layers with respect to the substrate is not well defined as visible from the diffraction rings in LEED. The rotational disorder and the absence of an interface layer indicate a rather weak coupling between the graphene layer and the substrate [43, 66]. This difference in growth mode also results in quite different electronic properties as compared to SiC(0001) [28].

Quite recently we have extended the analytical possibilities for epitaxial graphene to confocal Raman spectroscopy for micrometer scale analysis of layer thickness and graphene properties. With this method properties such as strain or defects as well as the carrier density but also the number of graphene layers can be analyzed with spatial resolution [42]. In this way it is possible to continuously monitor the epitaxial graphene layers during technological steps such as patterning or device preparation. As was shown in section 6.2 the SiC substrate induces an intrinsic doping of the graphene layers with negative charge carriers. This n-doping can be monitored by the position of the Dirac energy E_{D} in ARUPS [33]. A comparison of this result with the charge carrier concentration drawn from Raman spectroscopy by analysis of the G-peak position [42] shows good agreement. High resolution measurements of the π-bands and the position of the Dirac point allow us to study the electronic properties of the graphene samples in detail. Using transfer doping from molecules with high electron affinity we have been able to investigate possibilities for substrate doping compensation under well-defined conditions in UHV. In addition to the adjustment of charge neutrality we were able to achieve band structure engineering for thicker layers [69]. By depositing thin layers of Au on epitaxial graphene doping reversal could be induced and even p-type doping obtained. [70]. Atomic and molecular doping presents excellent perspectives for large scale fabrication of graphene-based devices. The techniques and results demonstrated in this paper allow a large variety of simple and precise experiments with few-layer epitaxial graphene. The results discussed here open up pathways to experiments to tune the electronic structure of graphene for future applications in carbon electronics.

References

[1] Wallace P R 1947 *Phys. Rev.* **71** 622
[2] Novoselov K S, Geim A K, Morozov S V, Jiang D, Zhang Y, Dubonos S V, Grigorieva I V and Firsov A A 2004 *Science* **306** 666
[3] Novoselov K S, Geim A K, Morozov S V, Jiang D, Katsnelson M I, Grigorieva I V, Dubonos A A and Firsov A A 2005 *Nature* **438** 197
[4] Zhang Y, Tan Y-W, Stormer H L and Kim P 2005 *Nature* **438** 201
[5] Geim A K and Novoselov K S 2007 *Nat. Mater.* **6** 183
[6] Peierls R E 1935 *Ann. Inst. H. Poincaré* **5** 177
[7] Landau L D 1937 *Phys. Z. Sowjetunion* **11** 26
[8] Ohta T, Bostwick A, Seyller T, Horn K and Rotenberg E 2006 *Science* **313** 951
[9] Emtsev K V, Seyller T, Speck F, Ley L, Stojanov P, Riley J D and Leckey R G C 2006 *Mater. Sci. Forum* **556/557** 525
[10] Semenoff G W 1984 *Phys. Rev. Lett.* **53** 2449
[11] Novoselov K S, McCann E, Morozov S V, Fal'ko V I, Katsnelson M I, Zeitler U, Jiang D, Schedin F and Geim A K 2005 *Nat. Phys.* **2** 177
[12] Katsnelson M I, Novoselov K S and Geim A K 2006 *Nat. Phys.* **2** 620
[13] Katsnelson M I and Novoselov K S 2007 *Solid State Commun.* **143** 3
[14] Berger C *et al* 2006 *Science* **312** 1191
[15] Ohta T, Bostwick A, McChesney J L, Seyller T, Horn K and Rotenberg E 2007 *Phys. Rev. Lett.* **98** 206802
[16] Zhou S Y, Gweon G-H, Fedorov A V, First P N, de Heer W A, Lee D-H, Guinea F, Castro Neto A H and Lanzara A 2007 *Nat. Mater.* **6** 770
[17] Rutter G M, Crain J N, Guisinger N P, Li T, First P N and Stroscio J A 2007 *Science* **317** 219
[18] Riedl C, Starke U, Bernhardt J, Franke M and Heinz K 2007 *Phys. Rev.* B **76** 245406
[19] van Bommel A J, Crombeen J E and van Tooren A 1975 *Surf. Sci.* **48** 463
[20] Mårtensson P, Owman F and Johansson L I 1997 *Phys. Status Solidi* b **202** 501
[21] Starke U, Schardt J and Franke M 1997 *Appl. Phys.* A **65** 587
[22] Starke U, Franke M, Bernhardt J, Schardt J, Reuter K and Heinz K 1998 *Mater. Sci. Forum* **264–268** 321
[23] Forbeaux I, Themlin J-M and Debever J-M 1998 *Phys. Rev.* B **58** 16396
[24] Simon L, Bischoff J L and Kubler L 1999 *Phys. Rev.* B **60** 11653
[25] Charrier A, Coati A, Argunova T, Thibaudau F, Garreau Y, Pinchaux R, Forbeaux I, Debever J-M, Sauvage-Simkin M and Themlin J-M 2002 *J. Appl. Phys.* **92** 2479
[26] Starke U 2004 Atomic structure of SiC surfaces *Silicon Carbide, Recent Major Advances* ed W J Choyke, H Matsunami and G Pensl (Berlin: Springer) pp 281–316
[27] Chen W, Xu H, Liu L, Gao X, Qi D, Peng G, Tan S C, Feng Y, Loh K P and Wee A T S 2005 *Surf. Sci.* **596** 176
[28] de Heer W A *et al* 2007 *Solid State Commun.* **143** 92
[29] Hass J, de Heer W A and Conrad E H 2008 *J. Phys.: Condens. Matter* **20** 323202

[30] Mattausch A and Pankratov O 2007 *Phys. Rev. Lett.* **99** 076802
[31] Varchon F *et al* 2007 *Phys. Rev. Lett.* **99** 126805
[32] Seyller T *et al* 2006 *Surf. Sci.* **600** 3906
[33] Riedl C, Zakharov A A and Starke U 2008 *Appl. Phys. Lett.* **93** 033106
[34] Lauffer P, Emtsev K V, Graupner R, Seyller T, Ley L, Reshanov S A and Weber H B 2008 *Phys. Rev.* B **77** 155426
[35] Vitali L, Riedl C, Ohmann R, Brihuega I, Starke U and Kern K 2008 *Surf. Sci.* **602** L127
[36] Hibino H, Kageshima H, Maeda F, Nagase M, Kobayashi Y and Yamaguchi H 2008 *Phys. Rev.* B **77** 075413
[37] Ohta T, El Gabaly F, Bostwick A, McChesney J L, Emtsev K V, Schmid A K, Seyller T, Horn K and Rotenberg E 2008 *New J. Phys.* **10** 023034
[38] Emtsev K V, Speck F, Seyller T, Ley L and Riley J D 2008 *Phys. Rev.* B **77** 155303
[39] Ni Z H, Chen W, Fan X F, Kuo J L, Yu T, Wee A T S and Shen Z X 2008 *Phys. Rev.* B **77** 115416
[40] Faugeras C, Nerrière A, Potemski M, Mahmood A, Dujardin E, Berger C and de Heer W A 2008 *Appl. Phys. Lett.* **92** 011914
[41] Röhrl J, Hundhausen M, Emtsev K V, Seyller T, Graupner R and Ley L 2008 *Appl. Phys. Lett.* **92** 201918
[42] Lee D S, Riedl C, Krauss B, v Klitzing K, Starke U and Smet J H 2008 *Nano Lett.* **8** 4320
[43] Varchon F, Mallet P, Magaud L and Veuillen J-Y 2008 *Phys. Rev.* B **77** 165415
[44] Hiebel F, Mallet P, Varchon F, Magaud L and Veuillen J-Y 2008 *Phys. Rev.* B **78** 153412
[45] Soubatch S, Saddow S E, Rao S P, Lee W Y, Konuma M and Starke U 2005 *Mater. Sci. Forum* **483–485** 761
[46] Starke U, Bram Ch, Steiner P-R, Hartner W, Hammer L, Heinz K and Müller K 1997 *Appl. Surf. Sci.* **89** 175
[47] Starke U, Bernhardt J, Schardt J and Heinz K 1999 *Surf. Rev. Lett.* **6** 1129
[48] Heinz K, Starke U, Bernhardt J and Schardt J 2000 *Appl. Surf. Sci.* **162/163** 9
[49] Starke U 2001 *Mater. Sci. Forum* **353–356** 205
[50] Starke U 2003 *Mater. Res. Soc. Proc.* **742** 35
[51] Heinz K, Bernhardt J, Schardt J and Starke U 2004 *J. Phys.: Condens. Matter* **16** S1705
[52] Starke U, Schardt J, Bernhardt J, Franke M, Reuter K, Wedler H, Heinz K, Furthmüller J, Käckell P and Bechstedt F 1998 *Phys. Rev. Lett.* **80** 758
[53] Schardt J, Bernhardt J, Starke U and Heinz K 2000 *Phys. Rev.* B **62** 10335
[54] Starke U, Schardt J, Bernhardt J, Franke M and Heinz K 1999 *Phys. Rev. Lett.* **82** 2107
[55] Starke U, Schardt J and Franke M 1997 *Appl. Phys.* A **65** 587
[56] Rutter G M, Guisinger N P, Crain J N, Jarvis E A A, Stiles M D, Li T, First P N and Stroscio J A 2007 *Phys. Rev.* B **76** 235416
[57] Stolyarova E, Rim K T, Ryu S, Maultzsch J, Kim P, Brus L E, Heinz T F, Hybertsen M S and Flynn G W 2007 *Proc. Natl Acad. Sci. USA* **104** 9209
[58] Brar W V, Zhang Y, Yayon Y, Ohta T, McChesney J L, Bostwick A, Rotenberg E, Horn K and Crommie M F 2007 *Appl. Phys. Lett.* **91** 122102
[59] Mallet P, Varchon F, Naud C, Magaud L, Berger C and Veuillen J-Y 2007 *Phys. Rev.* B **76** 041403(R)
[60] Latil D and Henrard L 2006 *Phys. Rev. Lett.* **97** 036803
[61] Riedl C and Starke U 2009 *Mater. Sci. Forum* at press http://www.fkf.mpg.de/ga/publications/preprints/C.Riedl.graphene.ECSCRM2008.pdf
[62] Emtsev K V *et al* 2009 *Nature Mater.* **8** 203
[63] Bernhardt J, Nerding M, Starke U and Heinz K 1999 *Mater. Sci. Eng.* B **61/62** 207
[64] Bernhardt J, Seubert A, Nerding M, Starke U and Heinz K 2000 *Mater. Sci. Forum* **338–342** 345
[65] Seubert A, Bernhardt J, Nerding M, Starke U and Heinz K 2000 *Surf. Sci.* **454–456** 45
[66] Hass J, Feng R, Millán-Otoya J E, Li X, Sprinkle M, First P N, de Heer W A, Conrad E H and Berger C 2007 *Phys. Rev.* B **75** 214109
[67] Forbeaux I, Themlin J-M and Debever J-M 1999 *Surf. Sci.* **442** 9
[68] Hoster H M, Kulakov M A and Bullemer B 1997 *Surf. Sci.* **382** L658
[69] Coletti C, Riedl C, Lee D S, v Klitzing K, Smet J H and Starke U 2009 in preparation
[70] Gierz I, Riedl C, Starke U, Ast C R and Kern K 2008 *Nano Lett.* **8** 4603